HHS Public Access

Author manuscript

ACS Catal. Author manuscript; available in PMC 2022 April 16.

Published in final edited form as:

ACS Catal. 2021 April 16; 11(8): 4381–4394. doi:10.1021/acscatal.0c05277.

Combined Theoretical and Experimental Investigation of Lewis Acid-Carbonyl Interactions for Metathesis

Tanmay Malakar,
Department of Chemistry, University of Michigan, Ann Arbor, Michigan 48109, United States

Carly S. Hanson,
Department of Chemistry & Biochemistry, Loyola University Chicago, Chicago, Illinois 60660, United States

James J. Devery III,
Department of Chemistry & Biochemistry, Loyola University Chicago, Chicago, Illinois 60660, United States

Paul M. Zimmerman
Department of Chemistry, University of Michigan, Ann Arbor, Michigan 48109, United States

Abstract

The coordination of a carbonyl to a Lewis acid represents the first step in a wide range of catalytic transformations. In many reactions it is necessary for the Lewis acid to discriminate between starting material and product, and as a result, how these structures behave in solution must be characterized. Herein, we report the application of computational modeling to calculate properties of the solution interactions of acetone and benzaldehyde with $FeCl_3$. Using these chemical models, we can predict spectral features in the carbonyl region of infrared (IR) spectroscopy. These simulated spectra are then directly compared to experimental spectra generated via titration-IR. We observe good agreement between theory and experiment, in that, between 0 and 1 equiv carbonyl with respect to $FeCl_3$, a pairwise interaction dominates the spectra. When >1 equiv carbonyl is present, our theoretical model predicts two possible structures composed of 4:1 carbonyl to $FeCl_3$, for acetone as well as benzaldehyde. When these predicted spectra are compared with titration-IR data, both structures contribute to the observed solution interactions. These findings suggest that the resting state of $FeCl_3$-catalyzed carbonyl-based reactions employing simple substrates starts as a Lewis pair, but this structure is gradually consumed and becomes a highly ligated, catalytically less active Fe-centered complex as the reaction proceeds.

Corresponding Authors: Paul M. Zimmerman – Department of Chemistry, University of Michigan, Ann Arbor, Michigan 48109, United States; paulzim@umich.edu; James J. Devery, III – Department of Chemistry & Biochemistry, Loyola University Chicago, Chicago, Illinois 60660, United States; jdevery@luc.edu.

Supporting Information

The Supporting Information is available free of charge at https://pubs.acs.org/doi/10.1021/acscatal.0c05277.
Computational details, bond order analysis, Mulliken charge analysis, solid state IR, spectral deconvolution analysis, and energies of all intermediate and transition states investigated (PDF)

Complete contact information is available at: https://pubs.acs.org/10.1021/acscatal.0c05277

The authors declare no competing financial interest.

An analytical model is proposed to quantify catalyst inhibition due to equilibrium between 1:1 and 4:1 carbonyl:Fe complexes.

Graphical Abstract

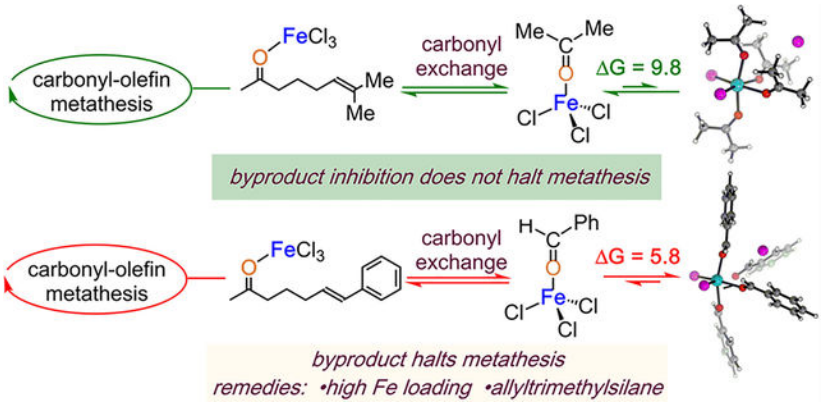

Keywords

carbonyl–olefin metathesis; iron catalysis; byproduct inhibition; carbonyl:Fe complexes

INTRODUCTION

Historically, transformations involving carbonyl compounds have played a crucial role in synthetic organic chemistry. Lewis acids (LA) have been employed ubiquitously to activate carbonyl-containing compounds in synthetic organic methods.[1–4] The underlying principle of LA activation operates via its ability to modify the electronic distribution of organic functionalities (e.g., carbonyls) that are capable of electron donation. Although the commonly accepted notion is that either the complex derived from a 1:1 Lewis pair (**1**)[5–13] or a 2:1 carbonyl-Lewis acid complex (**2**)[6,13–20] enables the reaction (Scheme 1a), the actual mode/structure that is responsible for the activation is not always obvious. For instance, Schindler et al. invoked alternative modes (**3**, **4**) of LA activation of aliphatic ketones via a singly bridged homobimetallic dimer (**4**, Scheme 1b).[21] Additionally, investigations involving simple carbonyls and LA carried out by the Devery lab revealed instances where LA can form complexes beyond the traditional 1:1 or 2:1 carbonyl-Lewis acid complexes (**5**, Scheme 1c).[22] Taken together, these findings guide our understanding of the mechanistic intricacies associated with LA-promoted reactions such as Diels–Alder reactions,[23] aldol reactions,[1,24,25] ene reactions,[26,27] and photochemical reactions.[28,29]

$FeCl_3$-mediated carbonyl-olefin metathesis is an efficient method to construct complex molecular scaffolds starting from simple molecular building blocks involving carbonyl and olefin functionalities.[30] In particular, this method has been successfully utilized in the synthesis of many cyclic motifs involving di- and trisubstituted cyclopentenes and cyclohexenes, polycyclic aromatic hydrocarbons,[31] and 2,5-dihydropyrroles.[32,33] Since then, a multitude of synthetic developments have expanded the utilization of Fe(III),[21,31–35] as well as employing Ga(III),[36,37] $BF_3{\cdot}OEt_2$,[38] montmorillonite, and I_2.[39] Mechanistic

investigations conducted by the Schindler, Zimmerman, and Devery groups identified that the catalytic cycle (Scheme 2) initiates through the generation of activated coordination complex **7** via interaction of the iron(III) chloride with the Lewis basic carbonyl moiety of **6**.[40] Complex **7** then isomerizes into oxetane intermediate **8** through a turnover limiting asynchronous, concerted [2 + 2]-cycloaddition. Subsequently, **8** fragments into cycloalkene product **9** and carbonyl byproduct-Fe(III)-complex (**1**) via a retro-[2 + 2] cycloaddition. Finally, carbonyl exchange turns the catalyst over. This last crucial step, while seemingly simple, has tremendous implications on the success of the catalytic mechanism: byproduct **10** is itself a Lewis base (LB) which can potentially bind to the LA catalyst. Indeed, our group and others have witnessed that byproduct inhibition hinders catalysis via inefficient carbonyl exchange and through the formation of alternative catalyst structures (**5**) that potentially remain catalytically active to a different degree.[41] Therefore, a detailed understanding of the solution behavior of the LA catalyst in the presence of substrate and carbonyl byproducts is needed to find reaction conditions that facilitate conversion of recalcitrant metathesis substrates.

Studying the solution behavior of the catalyst in a mixture of metathesis substrates and typical carbonyl byproducts is inherently complex due to potential competitive binding to the catalyst center. Although techniques like solid-state infrared (IR) spectroscopy and X-ray crystallography have proven useful in characterizing the interactions of LA and LB under stoichiometric conditions in the solid phase, experimental methods to characterize carbonyl-LA interactions in solution via in situ NMR are even more limited for paramagnetic Lewis acids. Recently, the Devery group developed a method relying on in situ solution-phase IR spectroscopy and solution conductivity to investigate the solution interactions between metal halide LA and simple carbonyl compounds such as acetone, benzaldehyde, and acetophenone.[22,41,42] With these detection methods, titrations into DCE containing LA as either a homogeneous solution (BF_3, BCl_3, $InCl_3$, $GaCl_3$, $TiCl_4$, and $SnCl_4$) or a heterogeneous slurry ($FeCl_3$, $AlCl_3$, and $ZrCl_4$), facets of the Lewis pair interactions were observed. For instance, while no ground state complexation for $ZnCl_2$ and $CeCl_3$ was detected, 1:1 classic Lewis pairs involving BF_3, BCl_3, $InCl_3$, and $GaCl_3$ were detected. Alternatively, 2:1 coordination complexes (**2**, Scheme 1a) were observed when simple carbonyl compounds were added to $TiCl_4$ and $SnCl_4$. Interestingly, highly ligated complexes (**5**, Scheme 1c) were formed when superstoichiometric amounts of carbonyl were added to $FeCl_3$ and $AlCl_3$. Additionally, these highly ligated structures resulted in an increase in the solution conductivity, consistent with some number of the chloride ligands being displaced from the metal center to the outer sphere. This effect had the consequence of allowing additional equivalents of carbonyl to add to the metal center. Importantly, these data suggest that the system under consideration has an appreciable equilibrium concentration of a new cationic species (**5**) that can potentially alter the metathesis reaction mechanism. This removal of chloride from the inner sphere of Fe(III) is similar to the behavior of homobimetallic association; however, unlike the LA-mediated chloride removal in the homobimetallic system, conditions leading to LB-mediated removal of chloride result in a decrease in reaction rate.

Because of this dichotomous complexity, an in-depth understanding of the thermodynamics of the superstoichiometric carbonyl addition and associated kinetics for the ligand displacement is still lacking. Further investigation is therefore warranted to achieve systematic guiding principles for efficient catalysis involving carbonyls and metal halides. Computational modeling is a powerful tool in investigating probable structures for LA complexes and their spectral features. Herein, careful computational modeling and IR deconvolution studies provide structural insight into the formation of the complexes that result from the addition of simple carbonyls (acetone and benzaldehyde) to LA ($FeCl_3$). We have chosen $FeCl_3$ as the model LA due to its high utility in carbonyl-olefin metathesis, and of equal importance, its unusual solution behavior in the presence of simple carbonyl compounds. In particular, we report that two possible structures composed of 4:1 carbonyl to $FeCl_3$ exist in the presence of superstoichiometric carbonyl, both of which contribute to the observed solution spectra. Furthermore, the implications of this highly ligated Fe-centered complex in inhibiting the catalytic activity are illustrated through an analytical model. This fundamental understanding of how the carbonyl specifically interacts with the LA in solution will promote the ability of synthetic chemists to develop efficient catalysis resulting in high yielding procedures.

Computational Details.

All quantum chemical calculations utilize density functional theory (DFT) as implemented in the Q-Chem 5.1 electronic structure program.[43] Geometry optimizations were carried out using the B97-D[44] density functional employing the double-ζ, 6–31+G* basis set. Initial transition state (TS) searches were performed using the reaction discovery tools of the Zimmerman group, in particular, the double-ended Growing String Method (GSM).[45–47] GSM locates minimum energy reaction paths and the associated transition states, without requiring detailed prior knowledge of the transition state structures. To ascertain the true nature of all stationary points, normal-mode analysis was conducted at the B97-D/6–31+G* level of theory. These frequency computations were further used to assign theoretical IR spectra of the predicted structures. Following this, single-point solvent phase calculations on the gas phase optimized geometries were performed using the SMD[48] solvent model, with 1,2-dichloroethane (DCE) as the solvent. SMD energies were computed using the ωB97X-D3[49] density functional and the def2-TZVP basis set in the ORCA quantum chemical package.[50] The solvent-phase free energies, G(l), were obtained by scaling the corresponding vibrational frequencies and gas-phase entropies S(g), in order to account for the rotational and translational degrees of freedom in the solvent phase. Noncovalent interaction (NCI) analysis was performed using the NCIPLOT program.[51,52] The high spin sextet state was found to be always lower in energy compared to other possible spin states (quartet, doublet) for all of the Fe^{3+} complexes investigated here. Reported energies for intermediates and activation barriers are solvent phase (DCE) free energies obtained using the ωB97X-D3/def2-TZVP level of theory in the sextet spin state (see S2 in the Supporting Information (SI) for full computational details).

RESULTS AND DISCUSSIONS

$FeCl_3$–Acetone System.

Titration-IR provides the ability to compare the relative amount of free carbonyl compound with the complex formed between acetone (**Ac**) and LA ($FeCl_3$, **Fc**). Under anhydrous conditions, **Fc** is largely insoluble in DCE, so **Ac** was titrated to a 12 mL slurry of **Fc** (2 mmol, Figure 1a) to bring **Fc** into solution. As **Ac** is added to the slurry, a concentration-dependent progression of observations occurs. Beginning from 0 to 1 equiv of **Ac**, a single vibration at 1633 cm^{-1} (Figure 1b) appears. Additionally, the system undergoes a phase transition from heterogeneity to homogeneity upon the addition of 1 equiv **Ac**, consistent with the formation of Lewis pair **A** in solution (see S3 in the SI for details).

Continued titration beyond 1 equiv **Ac** yields an isosbestic point at 1648 cm^{-1}, a decrease in the peak at 1633 cm^{-1}, an increase in the peak at 1714 cm^{-1} (free/unbound **Ac**), and the addition of a collection of vibrations intermediate between **Ac** and **A** (Figure 1c). These observations are consistent with the possible formation of a new species **B** beyond 1 equiv **Ac**. Inspection of the titration data suggests that the formation of species **B** requires three additional equivalents **Ac** to consume **A**, displacing a chloride to the outer sphere, which is consistent with conductivity measurements performed on the titration in parallel.[41] The system at 1 equiv **Ac**, however, displays similar spectral features as the system at 5 equiv **Ac**, suggesting that complex **A** is proceeding to a mixture of **A**, **Ac**, and **B** via a single observed transition about one isosbestic point.

To better understand the structure and characteristics of the **Fc** and **Ac** combination, quantum chemical modeling was carried out (see S4 in the SI). The investigations reveal that the formation of the tetrahedral 1:1 complex (**11**) from **Fc** and **Ac** is thermodynamically favorable (ΔG = −25.8 kcal/mol, ΔH = −29.9 kcal/mol) in DCE. Consistent with the large enthalpy of complex formation, the C=O stretching frequency of **11** is predicted to be significantly lower (1639 cm^{-1}) than that in free **Ac** (1738 cm^{-1}; Figure 2a, left). The stoichiometric composition and the C=O stretching frequency of **11** is consistent with the experimental observations in the region of 0–1 equiv of **Ac** (Figure 1b). Thus, it is reasonable to assign **11** as the structure of the 1:1 complex **A** (Figure 1a).

Next, reactions of **11** in the presence of higher equivalents of **Ac** were examined. Quantum chemical modeling suggests a trigonal bipyramidal 2:1 complex (**12**) is in equilibrium with **11**. The ΔG of formation of **12** from **11** is predicted to be only −2.4 kcal/mol (ΔH = −6.9 kcal/mol). The simulated C=O stretching frequencies in **12** are predicted to be at 1673 and 1679 cm^{-1} (Figure 2a, right).

Octahedral iron complexes with 3:1 **Ac**:**Fc** stoichiometry were then examined. Here, an octahedral iron complex where the third **Ac** lies trans to one of the chlorides was envisioned. No species of this type was found to be a stable intermediate, indicating that **12** cannot simply bind the third equivalent of **Ac**. To form a 3:1 **Ac**:**Fc** complex, simulations show that one of the chlorides needs to be detached from the inner coordination sphere of **12**, creating space for the third equiv of **Ac** in the inner coordination sphere of Fe. The migration of a chloride ion from the Fe center proceeds through **TS1** with an associated free energy barrier

of 20.4 kcal/mol ($\Delta H^{\ddagger}$ = 20.3 kcal/mol) and results in the tetrahedral complex **13** (see S5 in the SI), which is 19.1 kcal/mol uphill from **12** (ΔH = 18.3 kcal/mol, Figure 2b). Intermediate **13** is accessible mechanistically but not thermodynamically as its direct formation from **12** is significantly endoergic. However, the complexation process can pass through this intermediate to access more highly **Ac**-ligated Fe species that appear later on. Overall, the predicted mobility of chloride is consistent with the experimentally observed increase in solution conductivity beyond 1 equiv of **Ac** addition.[41]

Thus, our simulation shows that the 3:1 trigonal bipyramidal complex (**14**) lies 16.9 kcal/mol above **11** and free **Ac** in the free energy landscape (ΔH = 7.5 kcal/mol, Figure 3a). The theoretically simulated C=O stretching frequencies in **14** are predicted to be at 1669 and 1683 cm^{-1} (Figure 3a). Contrastingly, the third equiv of **Ac** in **14** results in a vibration appearing at 1318 cm^{-1} (see S6 in the SI), which is considerably red-shifted from the C=O vibration seen in free **Ac** (1738 cm^{-1}). This shift suggests that the strength of the C=O π bond of the third **Ac** ligand is significantly reduced, most likely due to substantial charge transfer from the nearby chloride ion (C−Cl distance 2.14 Å, Figure 3a) to the antibonding C=O π^* orbital.

The quantum chemical modeling studies predicted two possible structures (**15** and **16**) for the 4:1 Lewis complex. Species **15** is essentially a trigonal bipyramidal complex with a weakly associated **Ac** (see S4 in the SI). **15** is predicted to lie 17.5 kcal/mol above from **11** and **Ac** in the free energy landscape (Figure 3b, left). The weak coordination of the fourth **Ac** to the Fe center is evident from the longer bond distance (4.67 Å; Figure 3b, left) compared to the other three molecules of **Ac** (bond distances are 1.93, 2.23, and 2.31 Å). Noncovalent interaction (NCI) analysis of **15** indicates that the fourth **Ac** fits in the coordination pocket of Fe via dispersion interactions; whereas, the other three equiv of **Ac** are attached via strong interactions through lone-pair donation as displayed by green isosurfaces and blue disks, respectively, in Figure 4a. This inequivalency in the attachment of each **Ac** ligand is also reflected in the simulated IR spectra, where C=O stretching peaks exist at 1363, 1660, 1675, and 1712 cm^{-1} (Figure 3b, left). The appearance of the peak at 1712 cm^{-1} is consistent with the fourth equivalent of **Ac** being weakly bound. The remaining peak at 1363 cm^{-1} is associated with the strongly perturbed **Ac** by the nearby chloride ion (C−Cl distance 2.24 Å, Figure 3b, left) which is similar to that of species **14** (see S6 in the SI).

Alternatively to **15**, a second 4:1 complex (**16**) is octahedral and 7.7 kcal/mol more stable than **15** (Figure 3b, right). This observation is consistent with the NCI analysis of **16** which indicates that all four **Ac** ligands are coordinated to the Fe center via strong interactions through lone-pair donation as depicted by the blue disks in Figure 4b. Moreover, in sharp contrast to **15**, all four **Ac** ligands in **16** are in similar chemical environments indicated by their predicted C=O stretching peaks at 1657, 1659, 1666, and 1679 cm^{-1} (Figure 3b, right). Furthermore, the chloride ion in **16** is not bound to any particular chemical moiety, but instead is bound to the Fe complex by electrostatics. This predicted separation is consistent with the experimentally observed increase in solution conductivity upon superstoichiometric **Ac** addition. Note that although the predicted free energies indicate that there should be **12**

present in the reaction mixture, its discrete identification in the experiments is challenging as there is a significant overlap between theoretically simulated peaks of **12** (1673 and 1679 cm $^{-1}$) and **15**+**16** (1657, 1659, 1660, 1666, 1675, and 1679 cm^{-1}; see discussion S14 in SI).

$FeCl_3$–Benzaldehyde System.

Complexes generated from the interaction between **Fc** and the LB benzaldehyde (**Be**) were the next focus of our investigations. Titration-IR enabled comparison of the relative amount of free carbonyl compound with the complex formed from **Fc** and **Be** (Figure 5a). When 0–1 equiv of **Be** was added to a slurry of **Fc** (2 mmol) in DCE (12 mL), a single species with vibrations at 1610, 1592, and 1569 cm^{-1} was observed, and no unbound **Be** at 1704 cm^{-1} was detected (Figure 5b). Just like the combination of **Fc** and **Ac**, the system transitions from heterogeneity to homogeneity upon the addition of 1 equiv **Be**, suggesting the formation of 1:1 Lewis pair **C** (Figure 5a).

Complicated behavior was noted for titrations beyond 1 equiv of carbonyl. Continuation yields an isosbestic point at 1574 cm^{-1}, a decrease in the peak at 1569 cm^{-1}, and growing intensity in the peaks at 1577 and 1626 cm^{-1}. Simultaneously, the intensity of the signal for free/unbound **Be** grows at 1704 cm^{-1} and an additional collection of vibrations intermediate between **C** and **Be** appears (Figure 5c). A new species (**D**) is likely formed beyond 1 equiv **Be** (Figure 5a). Inspection of the titration data suggests that formation of species **D** requires three additional equiv **Be** to consume **C**, displacing a chloride to the outer sphere, which is consistent with conductivity measurements performed on the titration in parallel.[41] At 1 equiv **Be** the system displays similar spectral features as at 5 equiv **Be**, suggesting that complex **C** is proceeding to a mixture of **C**, **Be**, and **D** via a single transition with at least one isosbestic point at 1574 cm^{-1}.

Quantum chemical modeling provides further insights into the structure and characteristics of the complexes involving **Fc** and **Be**. The investigations reveal that the formation of tetrahedral 1:1 complex **17** from **Fc** and **Be** is highly thermodynamically favorable (ΔG = −21.8 kcal/mol, ΔH = −26.2 kcal/mol) in DCE. In unbound **Be**, along with the C=O vibration at 1716 cm^{-1}, there are two weakly absorbing peaks at 1600 and 1581 cm^{-1} due to C=C stretching vibrations in the aromatic ring. In the 1:1 Lewis pair **17**, however, these aromatic C=C peaks mix with the red-shifted C=O stretch. Therefore, unlike the Lewis pair complexes of **Ac**, three vibrations in the region of 1700–1500 cm^{-1} were observed for complexes involving **Be**. The three vibrations of **17** are predicted to be 1628, 1599, and 1569 cm^{-1}, and are generally lower in energy than those of free **Be** (1716, 1600, and 1581 cm^{-1}; Figure 6, left). The stoichiometric composition and the C=O stretching frequency of **17** is consistent with experimental observations in the region of 0–1 equiv of **Be** (Figure 5a). Thus, it is reasonable to assign **17** as 1:1 complex **C** (Figure 5a).

Reactions of **17** in the presence of higher equivalents of **Be** were considered next. Modeling suggests **17** transforms into a trigonal bipyramidal 2:1 complex (**18**) by addition of one **Be** with an associated ΔG of −5.4 kcal/mol (ΔH = −9.5 kcal/mol). The simulated C=O stretching frequencies in **18** are predicted to be 1660, 1653, 1602, 1601, 1577, and 1576 cm

$^{-1}$ (Figure 6, right). The close proximity of the theoretically predicted peaks, however, means these will not necessarily be individually resolvable in the experimental spectra.

Similar to **Ac**, simulation shows that species **18** can transform into a trigonal bipyramidal 3:1 complex (**19**), upon chloride migration from the inner sphere followed by coordination of the third equivalent of **Be** to the iron center. Species **19** lies 9.8 kcal/mol above **17** and free **Be** in the free energy landscape (ΔH = 1.1 kcal/mol, see S5 in the SI).

Just like with complexation of **Fc** with multiple equiv of **Ac**, quantum chemical modeling predicts two possible structures (**20** and **21**) for the 4:1 complex formed from **17** and **Be**. The complex (**20**) is analogous to species **15** and estimated to be 15.9 kcal/mol uphill in free energy (ΔH = 2.5 kcal/mol) from **17** and free **Be** (Figure 7, left). Interestingly, the other 4:1 complex (**21**) is analogous to species **16** and is 11.1 kcal/mol more stable than **20** (Figure 7, right). This observation is consistent with the NCI analysis of **21** which indicates that all four **Be** ligands are coordinated to the Fe center via lone-pair donation (blue disks in Figure 8). Moreover, in contrast to **20**, all four molecules of **Be** in **21** are coupled, indicated by their sequence of C=O stretching peaks between 1662 and 1552 cm^{-1}. Similar to **16**, the chloride ion in **21** is bound to the Fe complex by electrostatics, which is consistent with the experimentally observed increase in solution conductivity upon superstoichiometric addition of **Be**. Additionally, species **21** closely resembles the crystal structure obtained for **Fc** in the presence of excess **Be**.[41] The cationic Fe complex is balanced by $FeCl_4^-$ in the crystal structure. However, $FeCl_4^-$ formation would result in the composition of carbonyl:Fe to be 4:2, inconsistent with solution-phase stoichiometric observations (4:1) determined from component analysis of the titration-IR data. Moreover, the theoretically simulated IR spectra of the 4:1 complex involving the $FeCl_4^-$ displays a significant mismatch between the simulated and experimental spectra (see S15 in the SI for details). Overall, the $FeCl_4^-$ counteranion can be attributed to the crystallization process and is inconsistent with our solution-phase results.

Similar to **Ac**, we anticipate that the reaction system will be largely populated by species **21** at superstochiometric **Be** addition, since **21** is 11.1 kcal/mol more stable than **20**. Good agreement between the experimental results (ΔG = +5.2 kcal/mol) and the theoretically predicted Gibbs free energy (ΔG = +5.8 kcal/mol, Figure 7, right) for the formation of **21** from its precursor (see S11 in the SI for details) gives evidence that the computational modeling is an accurate representation of the possible solution structures formed in these systems.

Spectral Deconvolution of Titration-IR.

With a theoretical model in hand, we can corroborate our experimental observations with quantum chemical results. In order to interrogate the spectral results, it is necessary to determine which vibrations result in the observed spectra. For titration of **Fc** with **Ac**, from 0 to 1 equiv added **Ac**, a single band is observed in the carbonyl region at 1633 cm^{-1}. Alternatively, the incremental addition of **Be** to **Fc** yielded three bands in the carbonyl region at 1610, 1596, and 1573 cm^{-1} between 0 and 1 added **Be**. When titrations proceed

beyond 1 equiv added carbonyl, analysis of the resulting more complex spectra is less straightforward.

To accomplish the task of identifying bands in more complex spectra, spectral deconvolution was applied to the systems when >1 equiv carbonyl is present (Figure 9, top). The deconvolution of the experimental spectra is displayed as stacked plots, which contain an experimental spectrum (solid black), the spectrum that results from the combination of simulated peaks (dashed black), and the simulated components. Taking one of the spectra from Figure 1c, four individual components (I–IV) add together to a simulated spectrum in agreement with the original spectra, in this case where 0.265 M **Ac** is present in solution (Figure 9a). Deconvolution of spectra generated in the presence of 0.319, 0.383, 0.447, and 0.593 M **Ac** yielded the same peak centers for the four components within 1 cm^{-1}. Spectral bands I–III grow in intensity as the [**Ac**] increases. Band IV, which manifests at amounts of **Ac** less than 1 equiv with respect to **Fc** (Figure 1b), is consistent with Lewis pair **11** and decreases in intensity as [**Ac**] increases. Band I, at 1714.3 ± 0.3 cm^{-1}, is consistent with unbound **Ac**.

Spectral analysis on titration of **Fc** with **Be** (Figure 9, bottom) was also performed. In the carbonyl region of the IR (Figure 5c), 7 bands are required to approximate the spectrum (Figure 9f). Further, bands V–VII are present at amounts of **Be** less than 1 equiv with respect to **Fc** (Figure 5b) and are consistent with **17**. Band I is consistent with unbound **Be**. As the [**Be**] increases, bands I–IV increase in intensity and band V decreases, while maintaining the same peak centers at 1704.00 ± 0.00, 1685.00 ± 0.00, 1649.97 ± 0.03, 1629.5 ± 0.5, and 1611.3 ± 0.4 cm^{-1}, respectively. The peak centers of bands VI and VII shift to higher wavenumbers as [**Be**] increases, however, suggesting that the vibrations VI and VII in Figure 9f are different from those in Figure 9j.

Comparison of Theory and Experiment.

Having analyzed the individual vibrational components of the observed spectra, we then moved to compare these to the quantum chemical results. Since the absolute value of theoretically simulated peaks for the carbonyls and their corresponding 1:1 Lewis complex differs ~6–24 cm^{-1} from the experimentally observed spectra, the trend between theoretically predicted spectra and that of experiments was analyzed instead.

The predicted IR peaks based on the computed C=O vibrations for **Ac**, **11**, **15**, and **16** are therefore compared with the deconvoluted experimental spectra in Figure 10. In order to determine if there is a correlative agreement between our predicted and observed spectra, we began by assigning peaks. The predicted spectrum for **Ac** yields one peak which we assign to what is observed by titration-IR. The simulated spectrum for **11** predicts a single carbonyl vibration that is shifted to lower wavenumbers, which we observe in titration-IR. Between these two points are the vibrations for the structures that form at >1 equiv **Ac**. The two peaks our simulation predicts for **15** are consistent with bands II and III from our deconvoluted IR data. The simulated spectrum for **16** is also consistent with band III. Plotting the predicted IR vibration as a function of experimentally observed vibration yields a linear correlation with an $R^2 = 0.9754$ (Figure 10a). This correlation provides a mathematical relationship for

direct comparison of both data sets (Figure 10c). Bands I and IV are consistent with spectra predicted for **Ac** and **11**, respectively. Complex **16**, which our calculations predict is the more stable of the two possible 4:1 complexes, is consistent with band III. However, **16** does not align with band II, but complex **15** aligns with bands II and III. Though **16** is predicted to be the more stable than **15**, the combined theoretical and experimental results suggest that we are observing a mixture of **15** and **16** in solution at >1 equiv **Ac** addition, where band II is consistent with **15** and band III represents a combination of **15** and **16**.

Titration of **Fc** with **Be** displays more complex spectral behavior, which can be related to the quantum chemical model by focusing on the vibrations we can specifically identify. The simulated spectrum for **Be** is consistent with the C=O vibration observed for **Be** (Figure 10b). The prediction for **17** yields three IR peaks at lower wavenumbers relative to **Be**, which is consistent with titration-IR data, when **Fc** is in excess with respect to **Be**. For **20** and **21**, significant overlap exists between these predicted spectra, as well as the predicted spectrum for **17**, which is still present in the solution. This overlap is located between 1550 and 1625 cm^{-1}. However, spectral overlap decreases in the region between 1625 and 1690 cm^{-1}. In this region, **21** is predicted to have a vibration that is consistent with band III. Additionally, our prediction for **20** is consistent with bands II and IV. Like with the **Ac** data, plotting the predicted IR vibrations as a function of experimentally observed vibrations for the **Be** data yields a linear correlation with an $R^2 = 0.9934$ (Figure 10b). Again, the observed correlation assists in the direct comparison of both data sets (Figure 10d). Using this comparison, band I is consistent with **Be**. During our titrations, bands VI and VII shift as the [**Be**] increases. As a result, positive identification of these bands when **Be** is present in excess with respect to **Fc** is difficult. However, band V is consistent with the prediction of one of the vibrations of **17**. Similar to analysis of the **Ac**-based data, both 4:1 complexes are required to explain the observed IR bands. Thermodynamically more stable complex **21** is consistent with only band III, while **20** is consistent with both bands II and IV. Analogous to the **Ac** system, the combined theoretical and experimental results suggest there exists a mixture of **20** and **21** in solution with superstoichiometric **Be** addition. Previously, we were able to obtain a crystal of a complex from a solution of **Fc** and excess **Be**.[41] The X-ray crystal structure is consistent with the predicted structure of **21**, and the solid-state IR for the crystal is consistent with the spectrum predicted for **21**. This spectrum includes band III, but neither band II nor band IV is present (see S8 and S9 in the SI for more detail).

DISCUSSION

The combination of experiment and simulation yields the following model for complexation of carbonyls with **Fc**: (1) When **Fc** is present in excess with respect to **Ac**, the 1:1 Lewis pair **11** results. (2) The observed spectrum for **11** is in good agreement with the predicted spectrum. (3) When more **Ac** is added to a solution of **11**, Lewis pair **11** is consumed and converted to one or more structures with higher coordination numbers. (4) The predicted spectra for both **15** and **16** are required to assign all observed bands in the titration-IR data. (5) Titration of **Fc** with **Be** yields analogous results. Additionally, the kinetic examination of carbonyl-olefin metathesis shows that (6) **Ac**-producing **22** reaches full conversion with as little as 5 mol % **Fc** (Figure 11a); whereas, 50 mol % **Fc**, is required for **Be**-producing

reaction of **25** (Figure 11d).[41] (7) The addition of 50 mol % **Ac** or **Be** at the onset of the metathesis reaction of **22** or **25**, respectively, inhibits catalytic turnover. (8) The addition of 50 mol % **Be** (open red squares, Figure 11e) at the onset of the metathesis reaction of **25** resulted in relatively less product than when **Ac** is introduced to the reaction of **22** (open green squares, Figure 11b). (9) The ratio of **Ac** to **Fc** in the reaction of **22** is 10:1; whereas the ratio of **Be** to **Fc** at the onset of the reaction of **25** is 1:1. Taken together, these observations allow us to address how superstoichiometric amounts of **Ac** and **Be** impact the catalytic cycle of carbonyl-olefin metathesis by transforming the 1:1 complex into highly ligated carbonyl complex (**16**, **21**).

We have previously demonstrated that modification of the olefin partner in carbonyl-olefin metathesis-active substrates changes the mechanism of the reaction.[40] Further, we showed that changing the olefin of the substrate from one that produces **Ac** to one that produces **Be** can significantly decrease the yield. Li[33] and Schindler[21] have shown that the addition of allyltrimethylsilane to **Be**-producing reactions improves reaction outcomes by scavenging **Be** out of the reaction mixture. The reason for these alterations is likely to improve the efficiency of the ultimate step of the metathesis cycle: carbonyl exchange. Under stoichiometric conditions, metathesis substrate **22** can displace **Ac** from **24** (Figure 11c).[21] However, this exchange becomes difficult in the presence of superstoichiometric amounts of **Ac**, which inhibits the catalytic cycle. Likewise, the presence of **Be** inhibits catalytic turnover (Figure 11f). One question remains: what causes **Be**-producing reactions to require these procedural alterations?

EQUILIBRIUM MODEL FOR ACTIVE CATALYST CONCENTRATION

To understand the answer to this question, we first recognize that atomistic simulations predict that the conversion of Lewis pair **11** to tetra-ligated complex **16** (Figure 11c) is less favorable than conversion of **17** to **21** (Figure 11f) by 4.0 kcal/mol. Under equivalent conditions, metathesis reactions that produce **Be** can more easily access **21**, thus removing **Fc** from the active catalytic cycle and inhibiting product formation. To more precisely elucidate how activity varies with carbonyl byproduct formation, we fit an analytical model (see equilibrium expression in Figure 12 and S10 in the SI for details) to experimental data under the assumption that metathesis reactivity terminates when 99% of catalyst is consumed. For reaction of **28** with **Ac** byproduct (Figure 12), 56% yield at 1 mol % **Fc** and 99% yield at 5 mol % **Fc**[30] are consistent with an equilibrium constant of K_{Ac} = 0.00063 mol^{-3} L^3. Using K_{Ac}, the effective catalyst concentration $[\mathbf{Fe}]_{\mathbf{total}}$ can be determined as a function of substrate conversion (Figure 12a), where $[\mathbf{Fe}]_{\mathbf{total}}$ is the sum of all catalytically active Fe(III) species, including **Fc**, the **Fc-28** complex, and **11**. The plots for 1 mol % **Fc** (Figure 12a, blue) and 5 mol % **Fc** (Figure 12a, orange) show how catalyst loading impacts the relationship of $[\mathbf{Fe}]_{\mathbf{Total}}$ and conversion. When **Ac** byproducts are formed at 5 mol % catalyst loading, a significant amount of active catalyst is still left even after 99% conversion.

This analysis was applied to the reaction of **30** with **Be** byproducts.[40] We again calculate the equilibrium constant for formation of **21**, K_{Be} = 0.14 mol^{-3} L^3, applying the assumption that a 60% yield for the 5 mol % catalyst loading corresponds with 99% consumption of

complex **17** (Figure 12b, blue).[40] This model shows negligible consumption of **Fc** at a loading of 50 mol % (Figure 12b, orange), which is adequate to complete the reaction. The model also determines that a catalyst loading of 20 mol % **Fc** in the **Be**-producing reaction (Figure 12b, green) would provide an equivalent $[\mathbf{Fe}]_{\mathbf{Total}}$ at full conversion as that of the **Ac**-producing reaction (Figure 12a, orange). In other words, for **Be**-producing metathesis reactions, a 4-fold increase in the catalyst loading is required for high yielding procedures.

The analytical model is consistent with titration-IR observations, where 1) increasing the ratio of **Fc** to carbonyl byproduct increases the amount of Lewis pair (**11**) relative to highly aggregated complex (**16**) in solution and 2) metathesis substrate can efficiently access the Fe(III) center of the Lewis pair (**11**) via carbonyl exchange but is inhibited by the four equivalents of byproduct in complex (**16**).[41] Additionally, the model provides estimates of the impact of byproduct inhibition on the reaction rate as a function of the catalyst loading.

Next, the K_{Be}/K_{Ac} ratio (222) from the model (which was extracted from experimental data) corresponds to a relative free energy of inactive **Fc** formation, $\Delta\Delta G = 3.2$ kcal/mol. This value is in agreement with the quantum chemical prediction of $\Delta\Delta G = 4.0$ kcal/mol for the same quantity. Overall, this model's prediction of a decreased ΔG for the formation of **21** relative to **16** is consistent with the need for higher **Fc** loadings or chemical removal of byproduct **Be** from the reaction for high yielding reactions.

Finally, we examine the physical reason that **Be** converts **Fc** to cationic Fe complex **21** (Figure 11f) more easily than **Ac** drives **Fc** to the corresponding species **16** (Figure 11c). This difference likely is due to the ability of the ligand to better stabilize the charge on the Fe center in **21** vs **16** in the absence of the third chloride ion. In particular, distribution of charge across the four aromatic rings may be largely responsible for the $\Delta\Delta G$ of 4.0 kcal/mol compared to **Ac**, which has less atoms about which it can delocalize the excess charge. Mulliken charge analysis (see S18 in the SI for more details) provides support for this hypothesis. This explanation is in agreement with our previous report that found solution conductivity increases more with respect to each equivalent of **Be** (1130 ± 20 mS cm^{-1} per equiv **Be**) added as compared to **Ac** (450 ± 30 mS cm^{-1} per equiv **Ac**).[41] Overall, the quantum chemical model, kinetic model, and solution conductivity experiments are all consistent with **21** being more stable under equivalent conditions as the reaction progresses, therefore, exhibiting more pronounced inhibition than **16** (Figure 12).

CONCLUSION

The solution structures formed via coordination of **Ac** and **Be** to **Fc** were investigated based on theoretical modeling. For the interaction of **Ac** and **Fc**, our model predicts a pairwise interaction between **Ac** and **Fc** under stoichiometric conditions. When superstoichiometric amounts of **Ac** are present with respect to **Fc**, two solution structures composed of four molecules of **Ac** and one **Fc** result. Likewise, the model predicts a stoichiometric pairing of **Be** and **Fc** which transitions to two possible solution structures of 4:1 **Be** to **Fc**. These models allowed us to predict what spectral features would be observable in the infrared. Using these predictions, we see good agreement between the Lewis pairs **11** and **17** and spectra generated via titration-IR, which are observed when **Fc** is in excess relative to the

carbonyl. When **Ac** is in excess relative to **Fc**, our experimental spectra display vibrations consistent with a mixture of **Ac**, **11**, **15**, and **16** based on our model. A similar examination of **Be** and **Fc** reveals vibrations consistent with **Be**, **17**, **20**, and **21**. These findings are consistent with our previous proposal that these structures result in product inhibition of Fe-catalyzed carbonyl-olefin metathesis.[41] This work describing the solution structures, in concert with the report of Fe(III) dimers being active in the reaction of aliphatic carbonyls,[21] emphasizes that significant consideration of solution structures allows for a more complete understanding of reaction behavior in catalytic systems. Importantly, our theoretical model for the ground state interactions of carbonyls and $FeCl_3$ not only allows us to understand what is happening in solution in carbonyl-olefin metathesis but also provides an avenue for predicting the impact of alternative Lewis acids and ligand effects on ring-closing carbonyl-olefin metathesis. Because these unusual structures are likely a factor in many carbonyl-based $FeCl_3$-catalyzed reactions, we are currently examining alternative systems to understand the impact of the solution structures accessible to $FeCl_3$ in catalytic regimes.

Supplementary Material

Refer to Web version on PubMed Central for supplementary material.

ACKNOWLEDGMENTS

T.M. and P.M.Z. thank the NIH for support under R35-GM-128830. C.S.H. and J.J.D. thank the NIH/National Institute of General Medical Sciences (GM128126) for financial support.

REFERENCES

(1). Matsuo J; Murakami M The Mukaiyama Aldol Reaction: 40 Years of Continuous Development. Angew. Chem., Int. Ed 2013, 52 (35), 9109–9118.

(2). Modern Carbonyl Chemistry; Otera J, Ed.; Wiley-VCH Verlag GmbH, 2000.

(3). Yamamoto H; Ishihara K Acid Catalysis in Modern Organic Synthesis 2008, 2.

(4). Yamamoto H; Ishihara K Acid Catalysis in Modern Organic Synthesis; Yamamoto H, Ishihara K, Eds.; Wiley-VCH: Weinheim, Germany, 2008; Vol. 1.

(5). Sorrell TA Organic Chemistry, 2nd ed.; University Science Books, 2006.

(6). Lappert MF 174. Co-Ordination Compounds Having Carboxylic Esters as Ligands. Part I. Stoicheiometry, Structure, and Stereochemistry. J. Chem. Soc 1961, 817.

(7). Lappert MF 103. Co-Ordination Compounds Having Carboxylic Esters as Ligands. Part II. Relative Acceptor Strengths of Some Group III and IV Halides. J. Chem. Soc 1962, 542.

(8). Susz BP; Chalandon P Etude de Composés d'addition Des Acides de Lewis. IX. - Spectres d'absorption Infrarouge Des Composés Formés Par La Benzophénone et l'acétophénone Avec BF_3, $FeCl_3$, $ZnCl_2$ et $AlCl_3$ et Nature de La Liaison Oxygène-Mètal. Helv. Chim. Acta 1958, 41 (5), 1332–1341.

(9). Reetz MT; Hüllmann M; Massa W; Berger S; Rademacher P; Heymanns P Structure and Electronic Nature of the Benzaldehyde/Boron Trifluoride Adduct. J. Am. Chem. Soc 1986, 108 (9), 2405–2408. [PubMed: 22175591]

(10). Cook D Infrared Spectra of Xanthone: Lewis Acid Complexes. Can. J. Chem 1963, 41 (2), 522–526.

(11). Cook D The Interaction of Friedel–Crafts Catalysts With Organic Molecules: III. The CH_3COCl:$GaCl_3$ System. Can. J. Chem 1962, 40 (3), 480–485.

(12). Rosenheim A; Levy W Ueber Die Verbindungen Ungesättigter Ketone Mit Metallchloriden. Ber. Dtsch. Chem. Ges 1904, 37 (3), 3662–3671.

(13). Pfeiffer P; Halperin O; Pros E; Schwarzkopf V Additionsprodukte von Zinnhalogeniden an Carbonylverbindungen I. Beitrag Zur Theorie Der Halochromieerscheinungen. Justus Liebig's Ann. Chem 1910, 376 (3), 285–310.

(14). Chand Paul R; Chadha SL Structure of Donor-Acceptor Complexes-VIII. Complexes of Lewis Acids with Ketones. J. Inorg. Nucl. Chem 1969, 31 (6), 1679–1683.

(15). Lewis FD; Oxman JD; Huffman JC Photodimerization of Lewis Acid Complexes of Cinnamate Esters in Solution and the Solid State. J. Am. Chem. Soc 1984, 106 (2), 466–468.

(16). Denmark SE; Henke BR; Weber E $SnCl_4$(4-Tert-$BuC_6H_4CHO)_2$. X-Ray Crystal Structure, Solution NMR, and Implications for Reactions at Complexed Carbonyls. J. Am. Chem. Soc 1987, 109 (8), 2512–2514.

(17). Branchadell V; Oliva A Complexes between Formaldehyde and Titanium Tetrachloride. An Ab Initio Study 1992; Vol. 114.

(18). Bertinato P; Sorensen EJ; Meng D; Danishefsky SJ Studies toward a Synthesis of Epothilone A: Stereocontrolled Assembly of the Acyl Region and Models for Macrocyclization. J. Org. Chem 1996, 61 (23), 8000–8001. [PubMed: 11667778]

(19). Graven WM; Peterson RV Addition Compounds of $HfCl_4$ and $ZrCl_4$ with Organic Ligands. J. Inorg. Nucl. Chem 1969, 31 (6), 1743–1748.

(20). Galeffi B; Simard M; Wuest JD Coordination Chemistry of Zirconium Tetrachloride. Crystal Structure of the 1:2 Adduct with Pinacolone. Inorg. Chem 1990, 29 (5), 951–954.

(21). Albright H; Riehl PS; McAtee CC; Reid JP; Ludwig JR; Karp LA; Zimmerman PM; Sigman MS; Schindler CS Catalytic Carbonyl-Olefin Metathesis of Aliphatic Ketones: Iron(III) Homo-Dimers as Lewis Acidic Superelectrophiles. J. Am. Chem. Soc 2019, 141 (4), 1690–1700. [PubMed: 30596414]

(22). Hanson CS; Psaltakis MC; Cortes JJ; Siddiqi SS; Devery JJ Investigation of Lewis Acid-Carbonyl Solution Interactions via Infrared-Monitored Titration. J. Org. Chem 2020, 85 (0), 820. [PubMed: 31830419]

(23). Fochi M; Caruana L; Bernardi L Catalytic Asymmetric Aza-Diels-Alder Reactions: The Povarov Cycloaddition Reaction. Synthesis (Germany) 2014, 135–157.

(24). Mukaiyama T; Narasaka K; Banno K New Aldol Type Reaction. Chem. Lett 1973, 2 (9), 1011–1014.

(25). Gati W; Yamamoto H Second Generation of Aldol Reaction. Acc. Chem. Res 2016, 49 (9), 1757–1768. [PubMed: 27513812]

(26). Hoffmann HMR The Ene Reaction. Angew. Chem., Int. Ed. Engl 1969, 8 (8), 556–577.

(27). Carlos Dias L Chiral Lewis Acid Catalyzed Ene-Reactions. Curr. Org. Chem 2000, 4 (3), 305–342.

(28). Brimioulle R; Lenhart D; Maturi MM; Bach T Enantioselective Catalysis of Photochemical Reactions. Angew. Chem., Int. Ed 2015, 54 (13), 3872–3890.

(29). Skubi KL; Blum TR; Yoon TP Dual Catalysis Strategies in Photochemical Synthesis. Chem. Rev 2016, 116, 10035–10074. [PubMed: 27109441]

(30). Ludwig JR; Zimmerman PM; Gianino JB; Schindler CS Iron(III)-Catalysed Carbonyl-Olefin Metathesis. Nature 2016, 533 (7603), 374–379. [PubMed: 27120158]

(31). McAtee CC; Riehl PS; Schindler CS Polycyclic Aromatic Hydrocarbons via Iron(III)-Catalyzed Carbonyl-Olefin Metathesis. J. Am. Chem. Soc 2017, 139 (8), 2960–2963. [PubMed: 28221039]

(32). Groso EJ; Golonka AN; Harding RA; Alexander BW; Sodano TM; Schindler CS 3-Aryl-2,5-Dihydropyrroles via Catalytic Carbonyl-Olefin Metathesis. ACS Catal. 2018, 8, 2006–2011. [PubMed: 30276008]

(33). Ma L; Li W; Xi H; Bai X; Ma E; Yan X; Li Z FeCl3-Catalyzed Ring-Closing Carbonyl–Olefin Metathesis. Angew. Chem., Int. Ed 2016, 55 (35), 10410–10413.

(34). Ludwig JR; Watson RB; Nasrallah DJ; Gianino JB; Zimmerman PM; Wiscons RA; Schindler CS Interrupted Carbonyl-Olefin Metathesis via Oxygen Atom Transfer. Science 2018, 361 (6409), 1363–1369. [PubMed: 30262500]

(35). Riehl P; Nasrallah D; Schindler C Catalytic, Transannular Carbonyl-Olefin Metathesis Reactions. Chem. Sci 2019, 10, 10267–10274. [PubMed: 32110312]

(36). Albright H; Vonesh HL; Becker MR; Alexander BW; Ludwig JR; Wiscons RA; Schindler CS GaCl 3 -Catalyzed Ring-Opening Carbonyl–Olefin Metathesis. Org. Lett 2018, 20 (16), 4954–4958. [PubMed: 30052456]

(37). Djurovic A; Vayer M; Li Z; Guillot R; Baltaze J-P; Gandon V; Bour C Synthesis of Medium-Sized Carbocycles by Gallium-Catalyzed Tandem Carbonyl–Olefin Metathesis/Transfer Hydrogenation. Org. Lett 2019, 21 (19), 8132–8137. [PubMed: 31545619]

(38). Rivero-Crespo MÁ; Tejeda-Serrano M; Pérez-Sánchez H; Cerón-Carrasco JP; Leyva-Pérez A Intermolecular Carbonyl-Olefin Metathesis with Vinyl Ethers Catalyzed by Homogeneous and Solid Acids in Flow. Angew. Chem., Int. Ed 2020, 59, 3846–3849.

(39). Tran UPN; Oss G; Breugst M; Detmar E; Pace DP; Liyanto K; Nguyen TV Carbonyl–Olefin Metathesis Catalyzed by Molecular Iodine. ACS Catal. 2019, 9 (2), 912–919.

(40). Ludwig JR; Phan S; McAtee CC; Zimmerman PM; Devery JJ; Schindler CS Mechanistic Investigations of the Iron(III)-Catalyzed Carbonyl-Olefin Metathesis Reaction. J. Am. Chem. Soc 2017, 139 (31), 10832–10842. [PubMed: 28753008]

(41). Hanson C; Psaltakis M; Cortes J; Devery J III Catalyst Behavior in Metal-Catalyzed Carbonyl-Olefin Metathesis. J. Am. Chem. Soc 2019, 141 (30), 11870–11880. [PubMed: 31276383]

(42). Hanson CS; Devery JJ Characterizing Lewis Pairs Using Titration Coupled with In Situ Infrared Spectroscopy. J. Vis. Exp 2020, e60745.

(43). Shao Y; Gan Z; Epifanovsky E; Gilbert ATB; Wormit M; Kussmann J; Lange AW; Behn A; Deng J; Feng X; Ghosh D; Goldey M; Horn PR; Jacobson LD; Kaliman I; Khaliullin RZ; Kuś T; Landau A; Liu J; Proynov EI; Rhee YM; Richard RM; Rohrdanz MA; Steele RP; Sundstrom EJ; Woodcock HL; Zimmerman PM; Zuev D; Albrecht B; Alguire E; Austin B; Beran GJO; Bernard YA; Berquist E; Brandhorst K; Bravaya KB; Brown ST; Casanova D; Chang C-M; Chen Y; Chien SH; Closser KD; Crittenden DL; Diedenhofen M; DiStasio RA; Do H; Dutoi AD; Edgar RG; Fatehi S; Fusti-Molnar L; Ghysels A; Golubeva-Zadorozhnaya A; Gomes J; Hanson-Heine MWD; Harbach PHP; Hauser AW; Hohenstein EG; Holden ZC; Jagau T-C; Ji H; Kaduk B; Khistyaev K; Kim J; Kim J; King RA; Klunzinger P; Kosenkov D; Kowalczyk T; Krauter CM; Lao KU; Laurent AD; Lawler KV; Levchenko SV; Lin CY; Liu F; Livshits E; Lochan RC; Luenser A; Manohar P; Manzer SF; Mao S-P; Mardirossian N; Marenich AV; Maurer SA; Mayhall NJ; Neuscamman E; Oana CM; Olivares-Amaya R; O'Neill DP; Parkhill JA; Perrine TM; Peverati R; Prociuk A; Rehn DR; Rosta E; Russ NJ; Sharada SM; Sharma S; Small DW; Sodt A; Stein T; Stück D; Su Y-C; Thom AJW; Tsuchimochi T; Vanovschi V; Vogt L; Vydrov O; Wang T; Watson MA; Wenzel J; White A; Williams CF; Yang J; Yeganeh S; Yost SR; You Z-Q; Zhang IY; Zhang X; Zhao Y; Brooks BR; Chan GKL; Chipman DM; Cramer CJ; Goddard WA; Gordon MS; Hehre WJ; Klamt A; Schaefer HF; Schmidt MW; Sherrill CD; Truhlar DG; Warshel A; Xu X; Aspuru-Guzik A; Baer R; Bell AT; Besley NA; Chai J-D; Dreuw A; Dunietz BD; Furlani TR; Gwaltney SR; Hsu C-P; Jung Y; Kong J; Lambrecht DS; Liang W; Ochsenfeld C; Rassolov VA; Slipchenko LV; Subotnik JE; Van Voorhis T; Herbert JM; Krylov AI; Gill PMW; Head-Gordon M Advances in Molecular Quantum Chemistry Contained in the Q-Chem 4 Program Package. Mol. Phys 2015, 113 (2), 184–215.

(44). Grimme S Semiempirical GGA-Type Density Functional Constructed with a Long-Range Dispersion Correction. J. Comput. Chem 2006, 27 (15), 1787–1799. [PubMed: 16955487]

(45). Zimmerman PM Automated Discovery of Chemically Reasonable Elementary Reaction Steps. J. Comput. Chem 2013, 34 (16), 1385–1392. [PubMed: 23508333]

(46). Zimmerman PM Navigating Molecular Space for Reaction Mechanisms: An Efficient, Automated Procedure. Mol. Simul 2015, 41 (1–3), 43–54.

(47). Zimmerman PM Growing String Method with Interpolation and Optimization in Internal Coordinates: Method and Examples. J. Chem. Phys 2013, 138 (18), 184102. [PubMed: 23676024]

(48). Marenich AV; Olson RM; Kelly CP; Cramer CJ; Truhlar DG Self-Consistent Reaction Field Model for Aqueous and Nonaqueous Solutions Based on Accurate Polarized Partial Charges. J. Chem. Theory Comput 2007, 3 (6), 2011–2033. [PubMed: 26636198]

(49). Lin Y-S; Li G-D; Mao S-P; Chai J-D Long-Range Corrected Hybrid Density Functionals with Improved Dispersion Corrections. J. Chem. Theory Comput 2013, 9 (1), 263–272. [PubMed: 26589028]

(50). Neese F The ORCA Program System. Wiley Interdiscip. Rev.: Comput. Mol. Sci 2012, 2 (1), 73–78.

(51). Contreras-García J; Johnson ER; Keinan S; Chaudret R; Piquemal J-P; Beratan DN; Yang W NCIPLOT: A Program for Plotting Noncovalent Interaction Regions. J. Chem. Theory Comput 2011, 7 (3), 625–632. [PubMed: 21516178]

(52). Glendening ED; Landis CR; Weinhold F NBO 6.0: Natural Bond Orbital Analysis Program. J. Comput. Chem 2013, 34 (16), 1429–1437. [PubMed: 23483590]

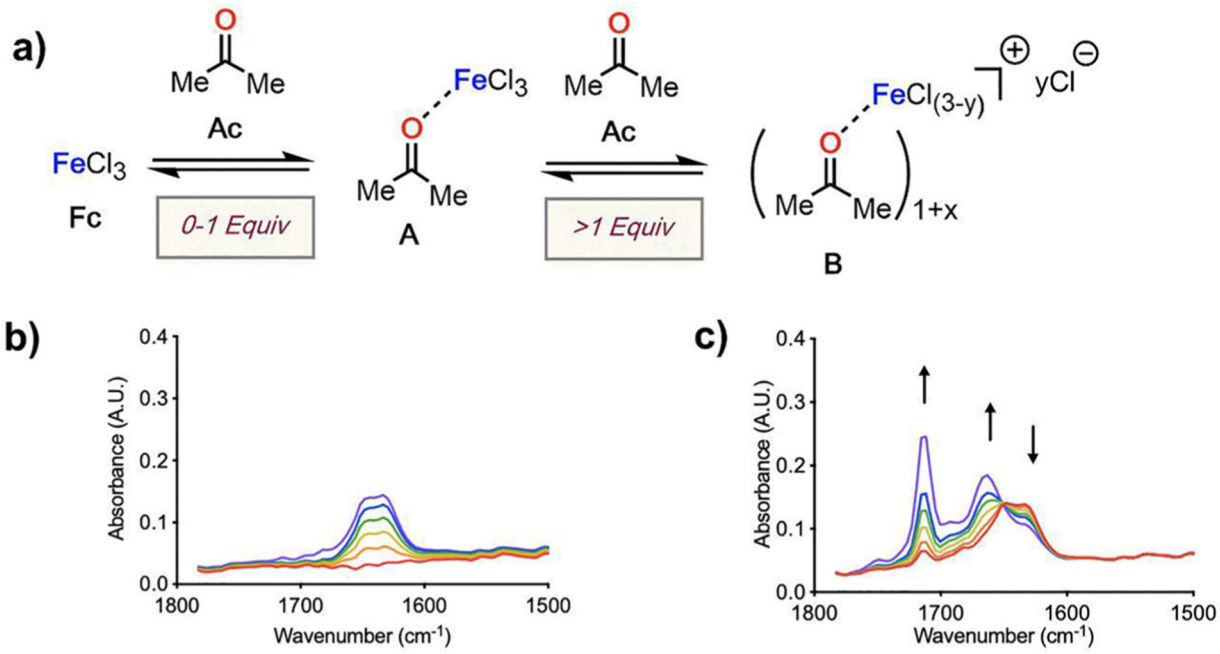

Figure 1.

(a) Proposed concentration-dependent interactions between **Fc** (2 mmol in 12 mL DCE) and **Ac**. (b) Solution IR spectra at 0–1 equiv **Ac** and (c) beyond 1 equiv **Ac** addition.

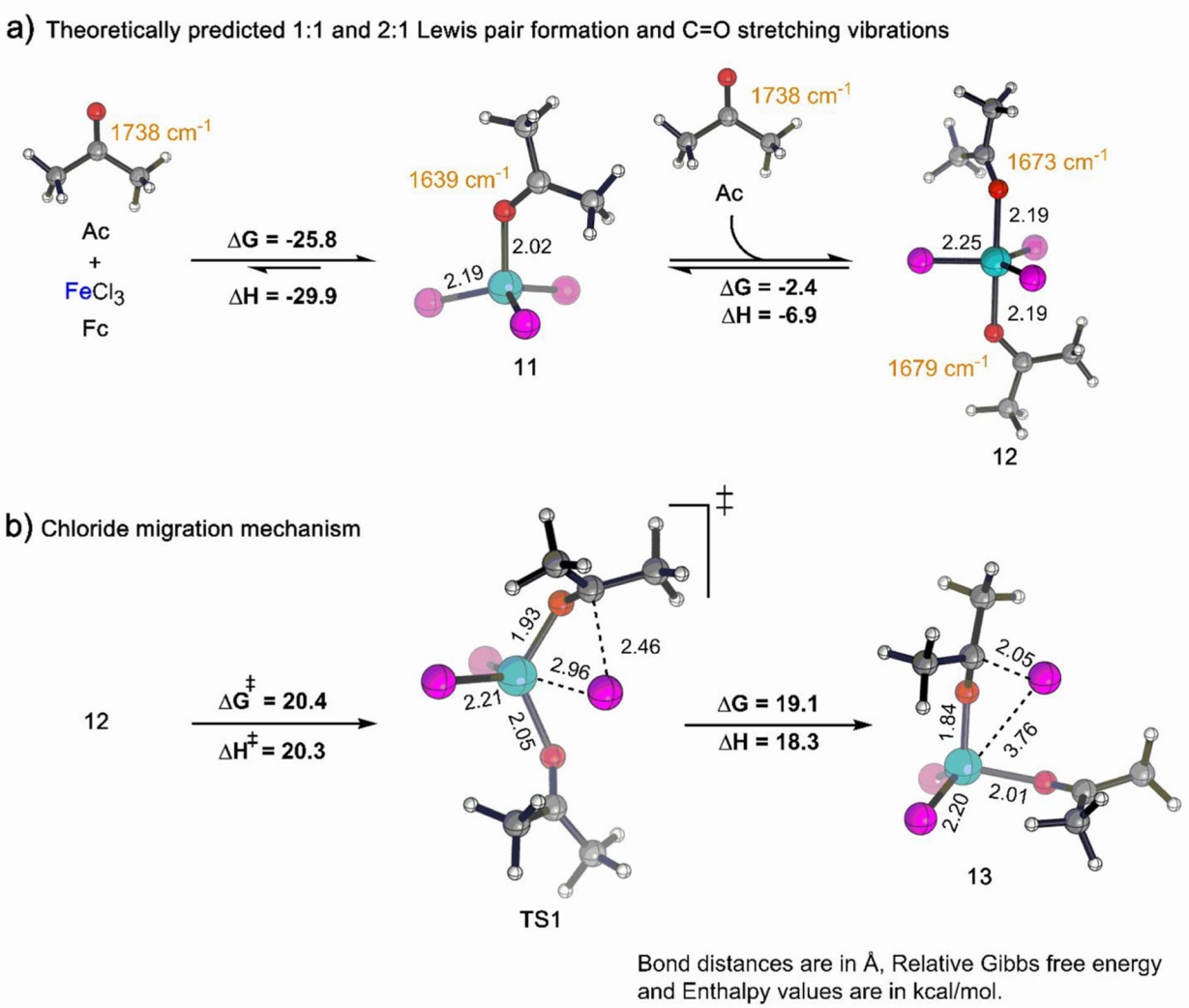

Figure 2.

Theoretically predicted thermodynamics and C=O IR stretching frequency (cm^{-1}) of (a) 1:1 and 2:1 complex formed from **Fc** and **Ac** and (b) thermodynamics of chloride migration. Reaction energies (kcal/mol) were obtained at ωb97X-D3/def2-TZVP/SMD(DCE) level of theory. Color code: Fe, cyan; Cl, magenta; O, red; C, gray; H, white.

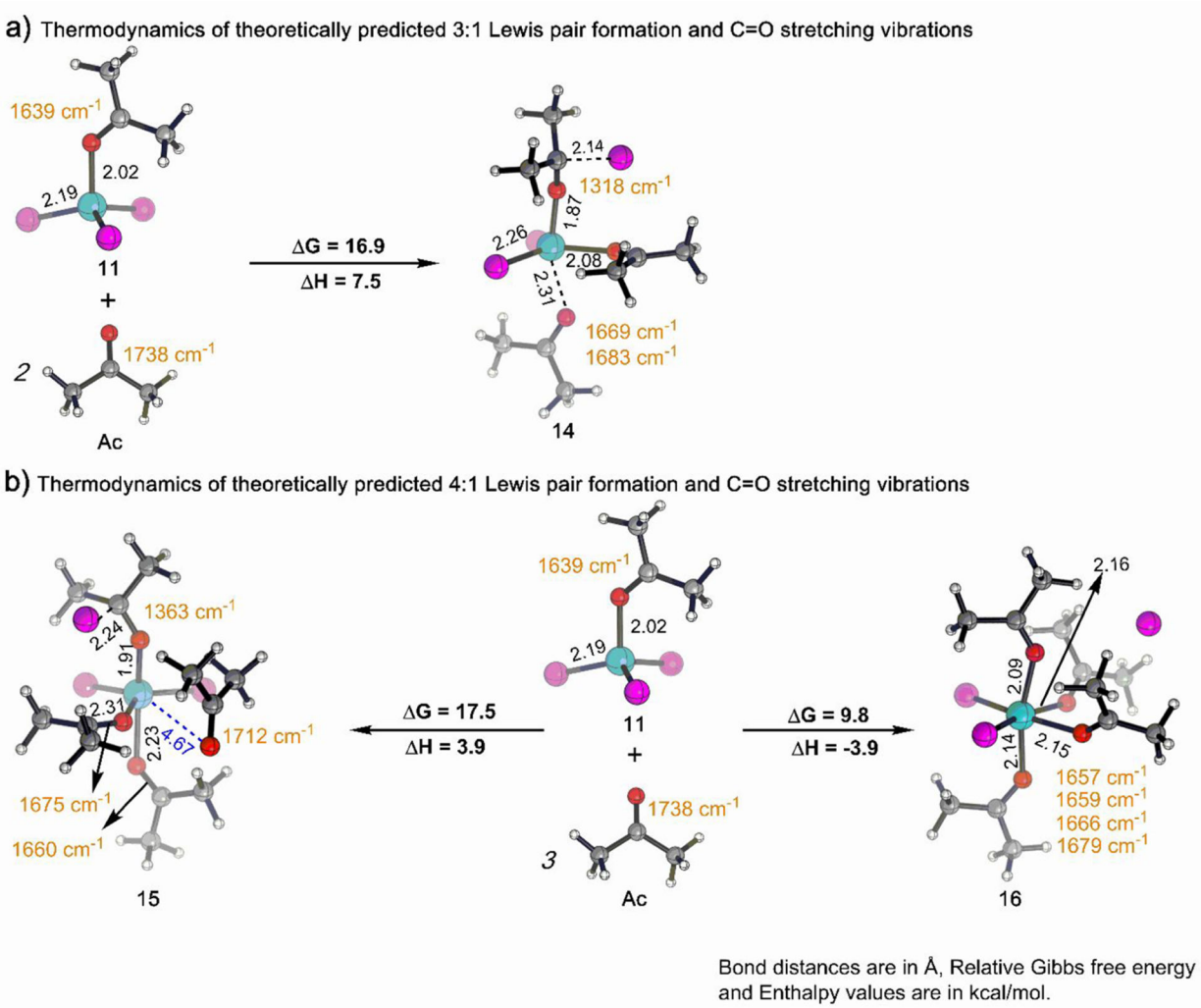

Figure 3.

Theoretically predicted thermodynamics and C=O IR stretching frequency (cm^{-1}) of (a) 3:1 and (b) 4:1 complex formed from **Fc** and **Ac**. Reaction energies (kcal/mol) were obtained at ωb97X-D3/def2-TZVP/SMD(DCE) level of theory. Color code: Fe, cyan; Cl, magenta; O, red; C, gray; H, white.

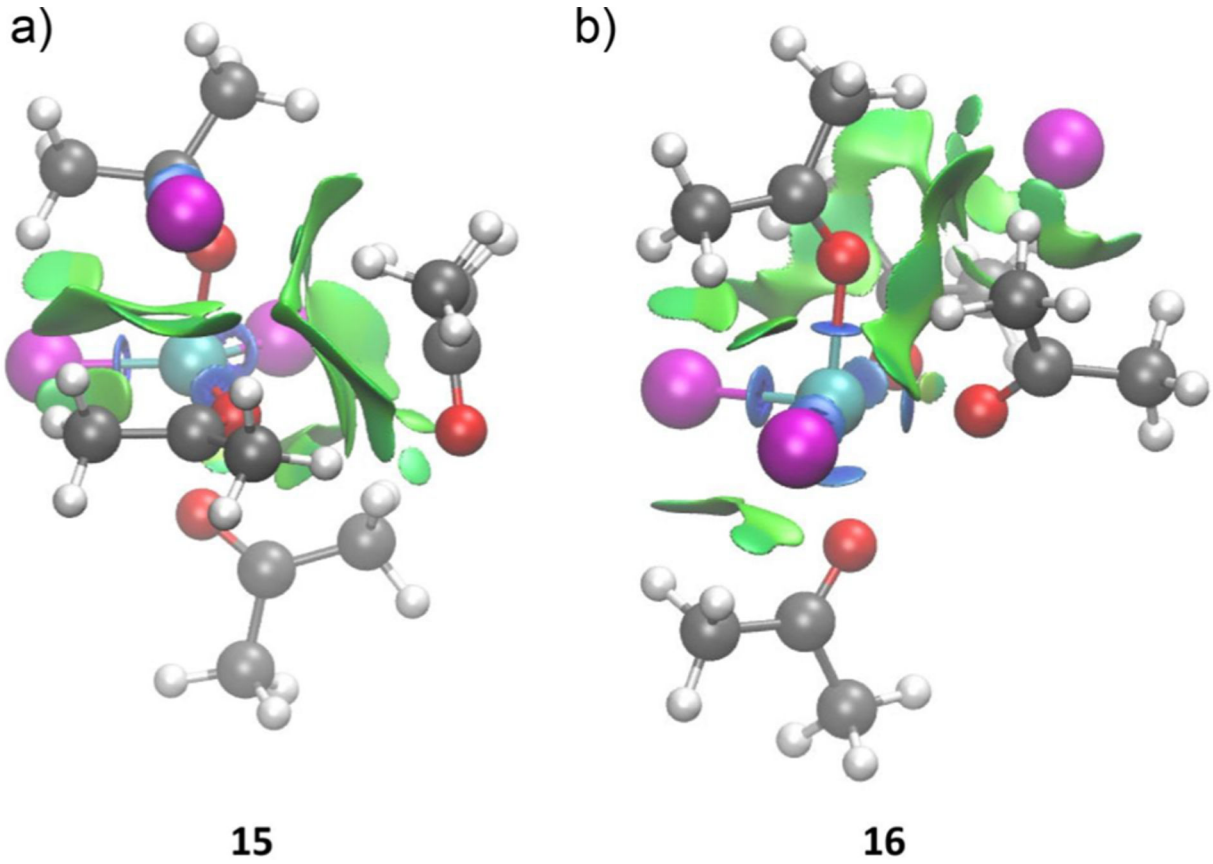

Figure 4.
NCI surfaces of species (a) **15** and (b) **16**. Color code: Fe, cyan; Cl, magenta; O, red; C, gray; H, white.

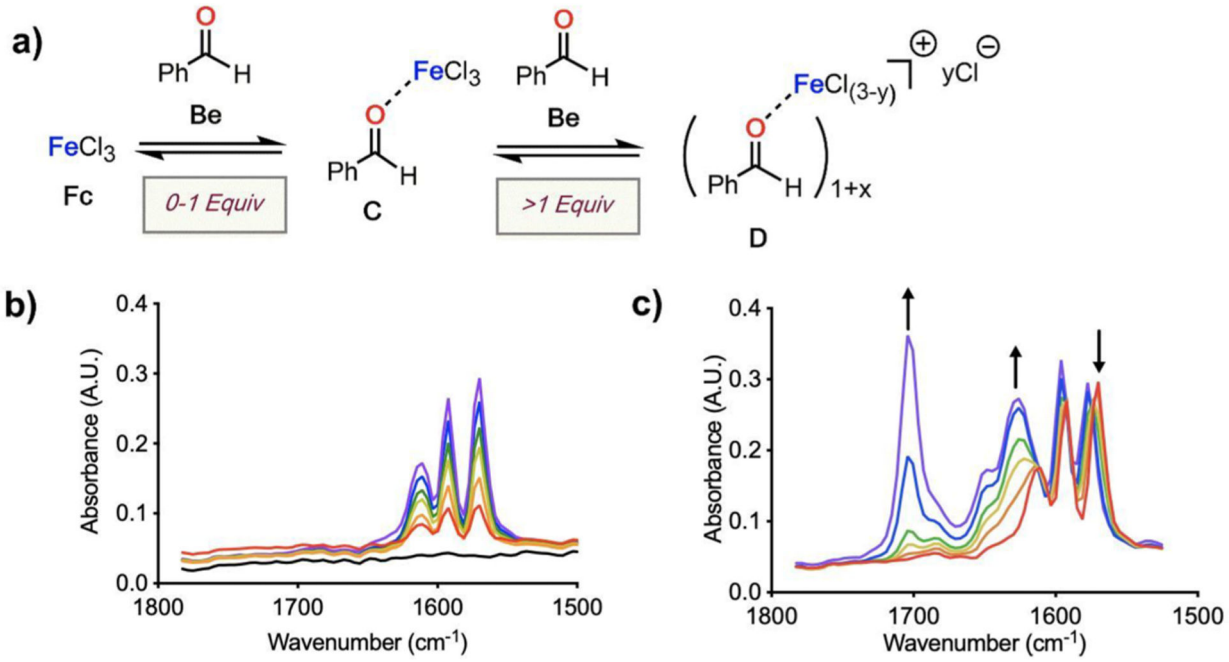

Figure 5.

(a) Proposed concentration-dependent interactions complexes between **Fc** (2 mmol in 12 mL DCE) and **Be**. (b) Solution IR spectra at 0–1 equiv **Be** and (c) beyond 1 equiv **Be** addition.

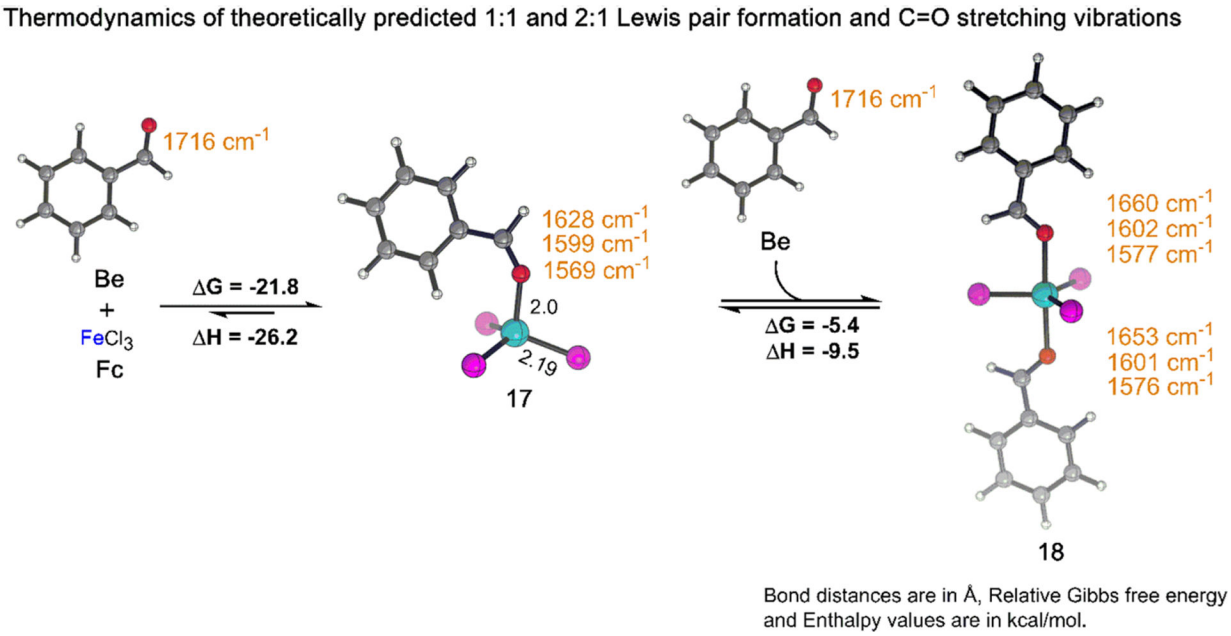

Figure 6.

Theoretically predicted thermodynamics and C=O IR stretching frequency (cm^{-1}) of 1:1 and 2:1 complex formed from **Fc** and **Be**. Reaction energies (kcal/mol) were obtained at ωb97X-D3/def2-TZVP/SMD(DCE) level of theory. Color code: Fe, cyan; Cl, magenta; O, red; C, gray; H, white.

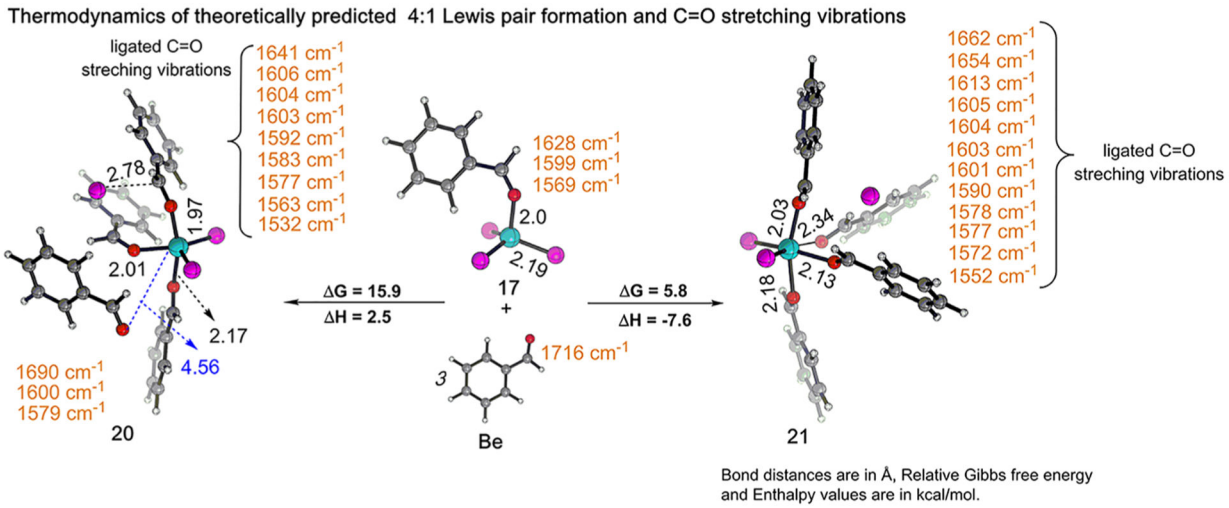

Figure 7.

Theoretically predicted thermodynamics and C=O IR stretching frequency (cm^{-1}) of 4:1 complex formed from **Fc** and **Be**. Reaction energies (kcal/mol) were obtained at ωb97X-D3/def2-TZVP/SMD(DCE) level of theory. Color code: Fe, cyan; Cl, magenta; O, red; C, gray; H, white.

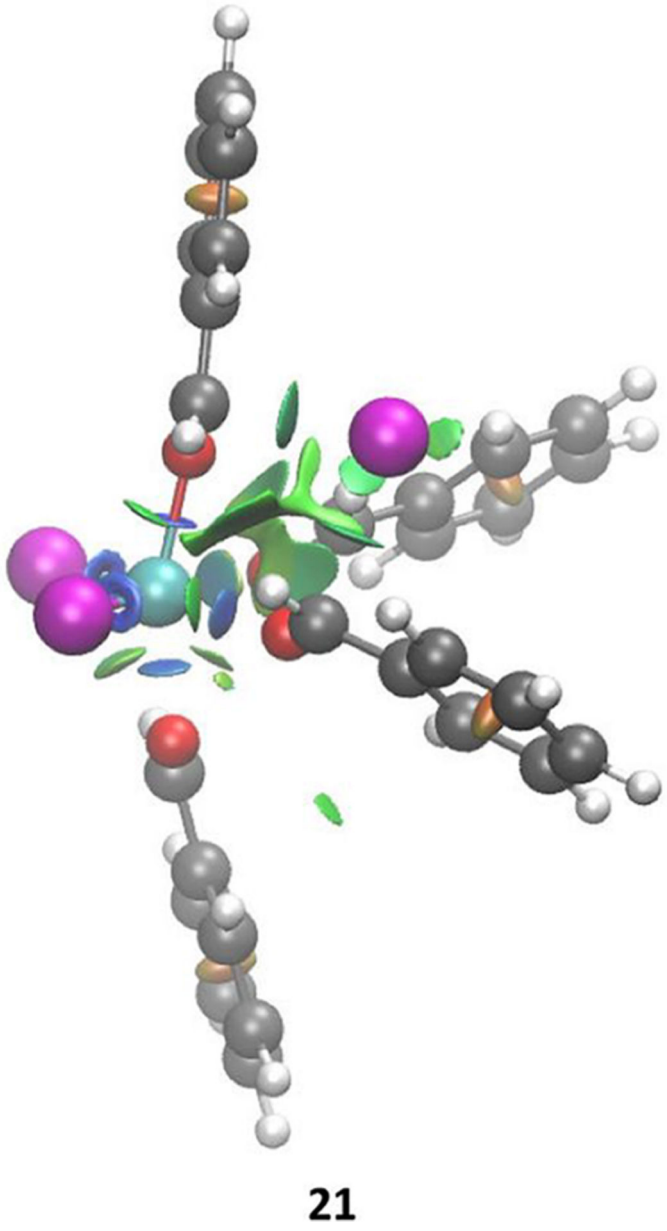

Figure 8.
NCI surfaces of **21**. Color code: Fe, cyan; Cl, magenta; O, red; C, gray; H, white.

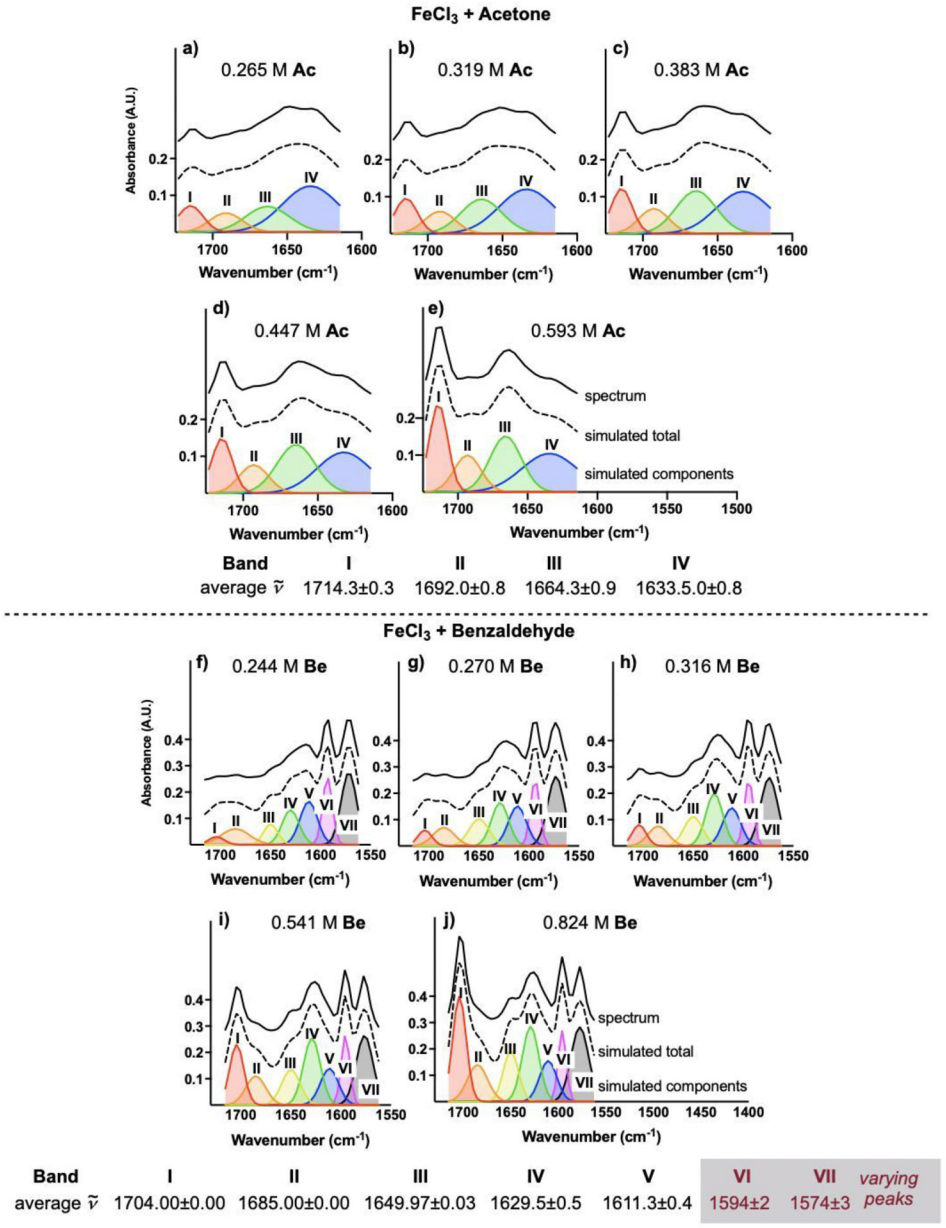

Figure 9.

Stacked plots of spectral deconvolution of titration of **Fc** (2 mmol in 12 mL DCE) with **Ac** (top) and titration of **Fc** (2 mmol in 12 mL DCE) with **Be** (bottom). Depicted *y*-axes list absorbance for simulated components.

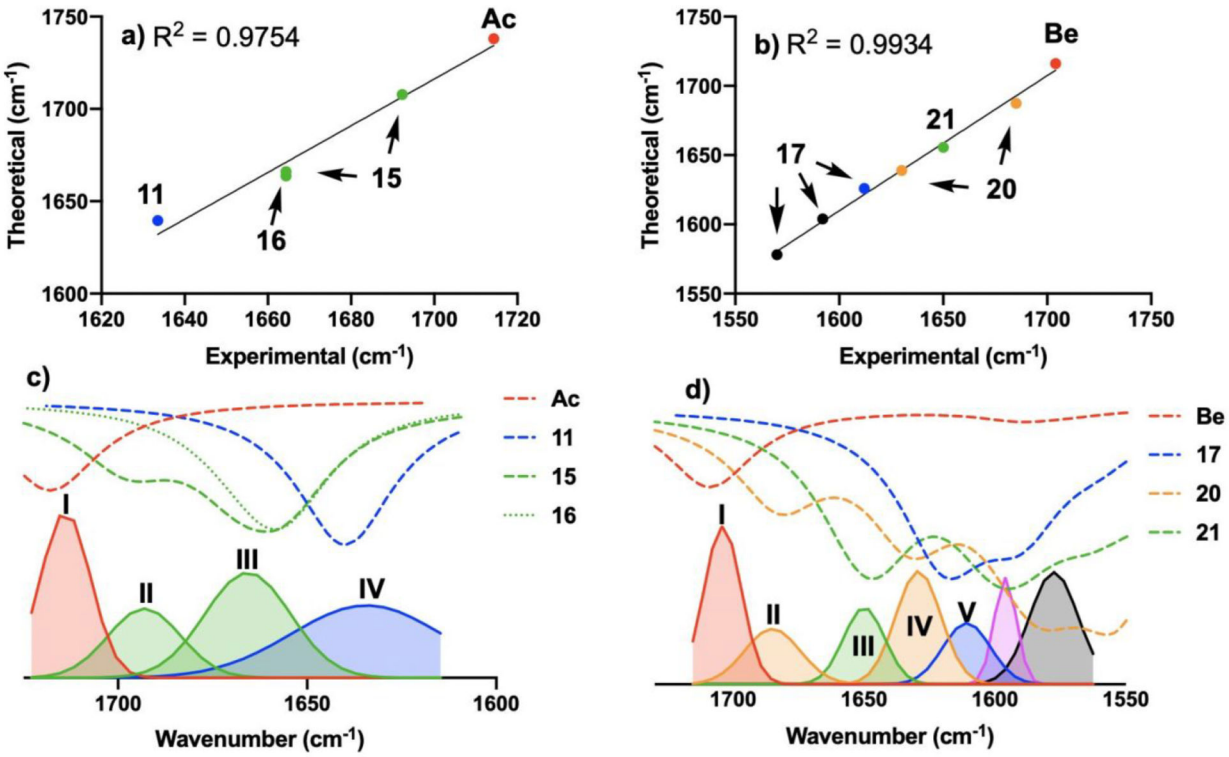

Figure 10.

(a) Correlation of theoretical IR vibrations with deconvoluted experimental vibrations for complexes of **Fc** and **Ac**. (b) Correlation of theoretical IR vibrations with deconvoluted experimental vibrations for complexes of **Fc** and **Be**. (c) Comparison of deconvoluted vibrations (solid lines) with correlation-corrected simulated spectra (dashed lines) for a mixture of **Fc** and 0.593 M **Ac**. (d) Comparison of deconvoluted vibrations (solid lines) with correlation-corrected simulated spectra (dashed lines) for a mixture of **Fc** and 0.824 M **Be**.

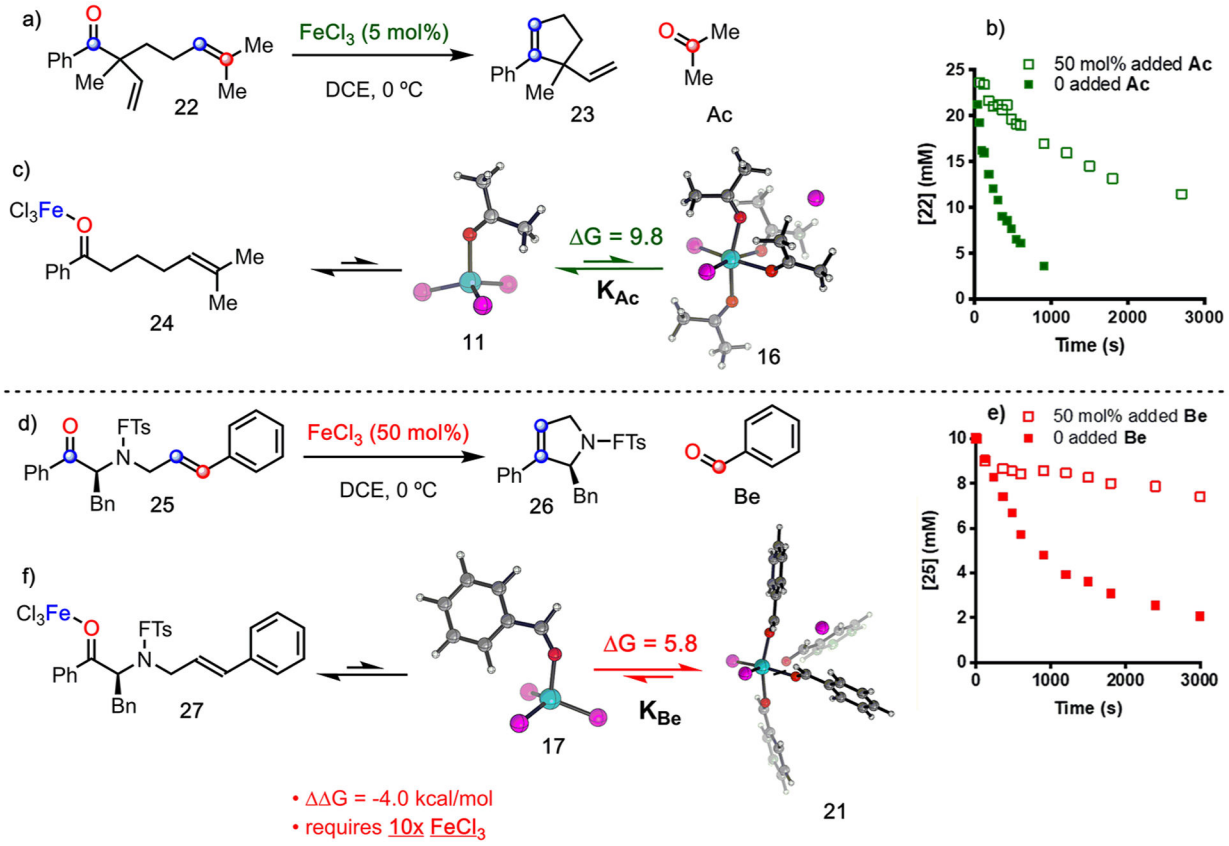

Figure 11.

(a) Carbonyl-olefin metathesis reaction of **22**. (b) [**22**] vs time for reaction of **22** (green ■). [**22**] vs time for reaction of **22** with 50 mol % **Ac** (green □).[41] (c) Efficient carbonyl-exchange in catalytic carbonyl-olefin methathesis when the byproduct is **Ac**. (d) Carbonyl-olefin metathesis reaction of **15**. (e) [**25**] vs time for reaction of **25** (red ■). [**25**] vs time for reaction of **25** with 50 mol % **Be** (red □).[41] (f) catalyst inhibition when the byproduct is **Be**. Free energies (kcal/mol) were obtained at ω*b*97X-D3/def2-TZVP/SMD(DCE) level of theory. Color code: Fe, cyan; Cl, magenta; O, red; C, gray; H, white.

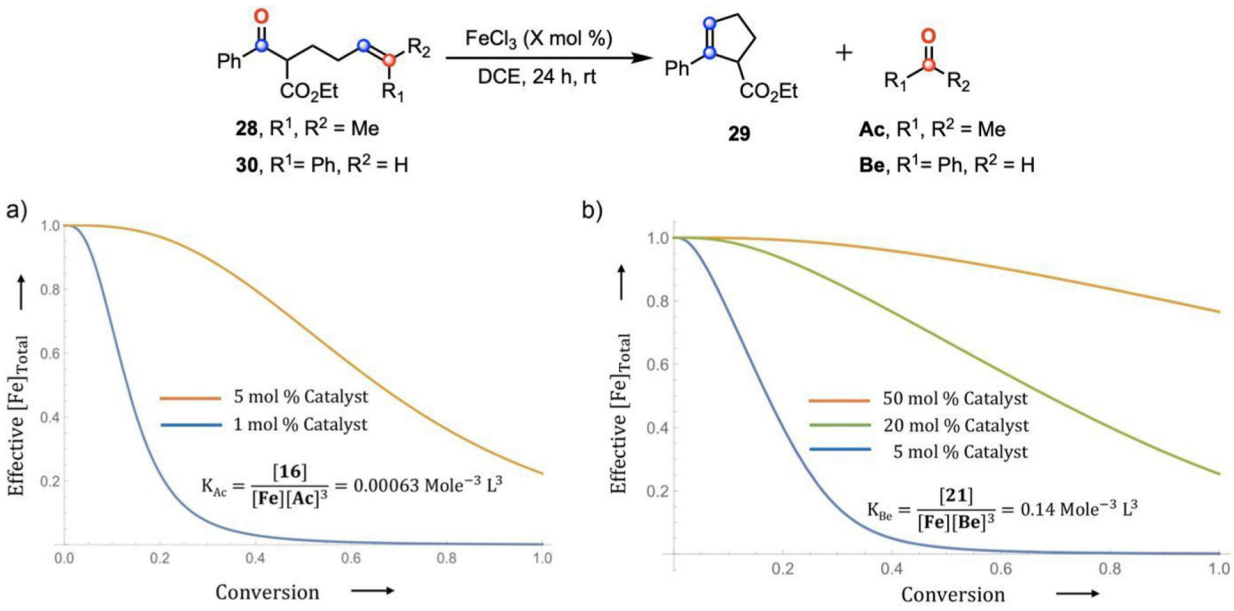

Figure 12.

Comparative catalyst inhibition in carbonyl-olefin metathesis involving (a) **Ac** producing substrate (**28**) and (b) **Be** producing substrate (**30**) with varied catalyst loading.

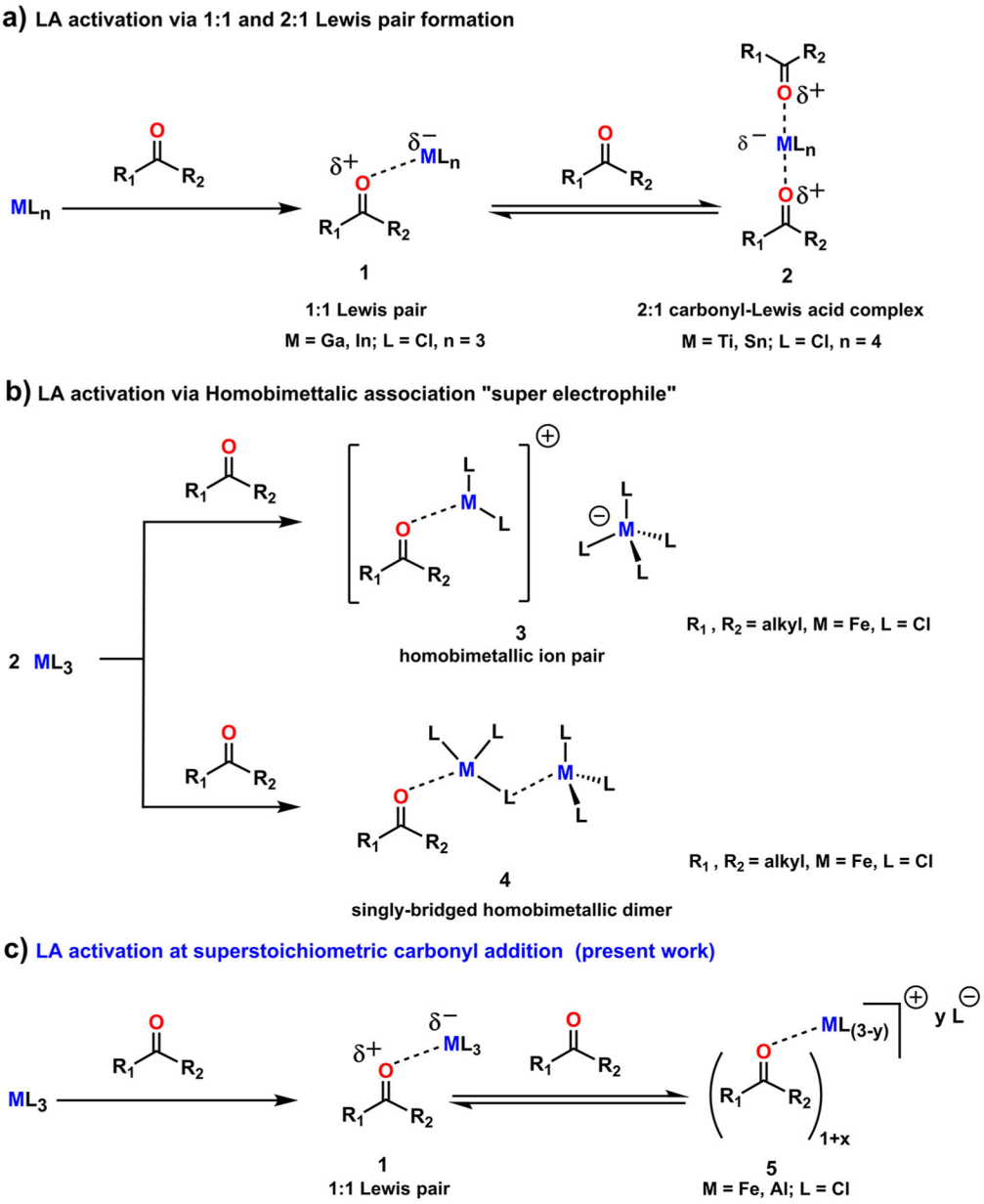

Scheme 1.

Different Modes of LA Activation of Carbonyl Substrate: (a) Classic Understanding of LA Activation via 1:1 and 2:1 Lewis Acid Complex Formation, (b) LA Activation via Homobimetallic Association, (c) LA Activation in the Presence of Superstochiometric Carbonyl in Solution

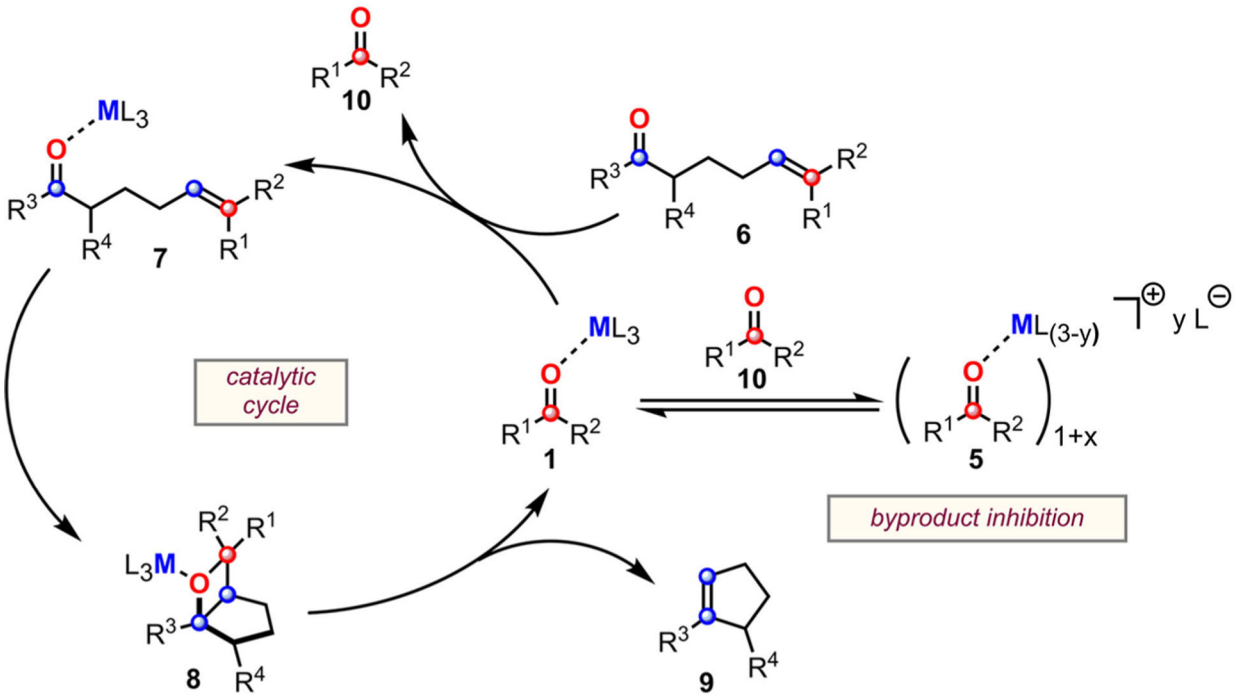

Scheme 2.
Proposed Mechanism of Carbonyl-Olefin Metathesis and Byproduct Inhibition